Electronic Supplementary Material (ESI) for Materials Horizons.

Supplementary Information

Highly Degenerate 2D Ferroelectricity in Pore Decorated Covalent/Metal Organic Frameworks.

*Lei Zhang [1,2], Cheng Tang [1,2], Stefano Sanvito [3], Aijun Du [*1,2]*

[1] School of Chemistry and Physics, Queensland University of Technology, Gardens Point Campus, Brisbane, QLD 4000, Australia

[2] Centre for Materials Science, Queensland University of Technology, Gardens Point Campus, Brisbane, QLD 4000, Australia

[3]School of Physics and CRANN Institute, Trinity College, Dublin 2, Ireland

Computational Details

The density functional theory (DFT) calculations were carried out using the Vienna ab initio simulation package (VASP).[1-3] The projector augmented wave (PAW) method[4] and the generalized gradient approximation (GGA) parameterized by Perdew, Burke, and Ernzerhof (PBE) [5, 6] were adopted in our calculations. The vdW interaction was taken into account by the DFT-D3 scheme.[7] The GGA+U method was applied to the 3*d* electrons of Cr, where the effective onsite Cpulomb interaction parameter (*U*) and exchange interaction parameter (*J*) are set to 3.0 and 1.0 eV, respectively, which were used in previous studies and well produce the magnetic exchange energy for $[Cr(pyz)_4]^{2-}$ fragments.[8] The cutoff energy for the plane-wave expansion was set to 520 eV and a k-point mesh of 5 × 5 ×1 was applied. The convergence criteria of residual forces and the energy were set as 0.01 eV/Å and 1×10^{-6} eV, respectively.[8] A vacuum region always larger than 15 Å was introduced to avoid the interaction between the neighboring periodic images.

The Heyd-Scuseria-Ernzerhof hybrid functional (HSE06) was utilized to obtain accurate electronic structures.[9] The climbing nudged elastic band (cNEB) method [10] was employed to study the FE phase transition. Ab initio molecular dynamics (AIMD) simulations were carried out for a total of 10 ps with a time step of 1 fs and the Langevin thermostat was applied to control the temperature.[11] The phonon spectra are calculated using the PHONOPY code with the machine-learning interatomic potentials—moment tensor potentials (MTPs) applied to calculate the force.[12-14] The nearest exchange interaction parameter can be derived based on the following Ising sipin Hamiltonian:

$$H = \sum JS_iS_j$$

where |S| is chosen as 2 and 1/2 for Cr atoms and pyrazine molecules, respectively. In this Hamiltonian, positive *J* suggests the antiferromagnetic coupling while negative *J* indicates the ferromagnetic coupling.

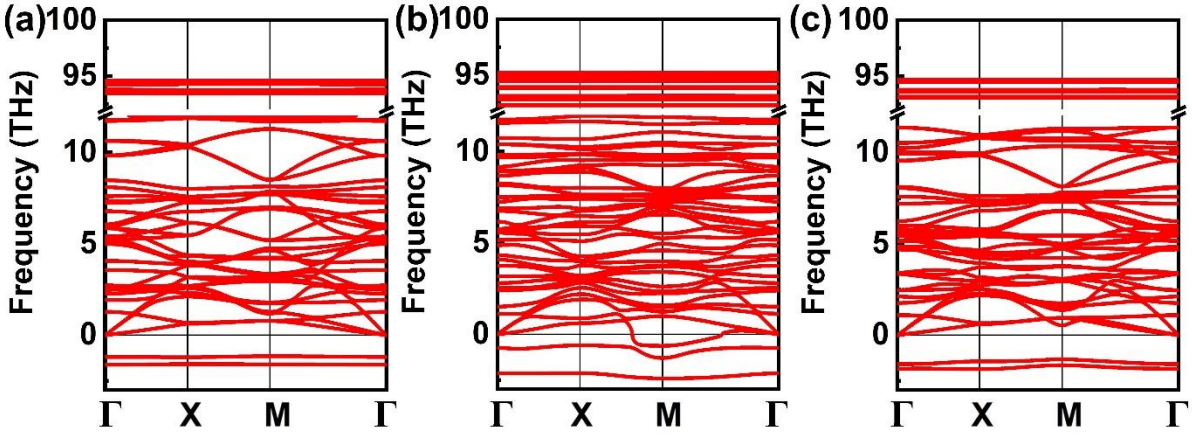

Figure S1. (a)-(c) The phonon spectra of $Li_{0.5}Cr(pyz)_2$ with Li anchored at B, C, and D Li adsorption sites.

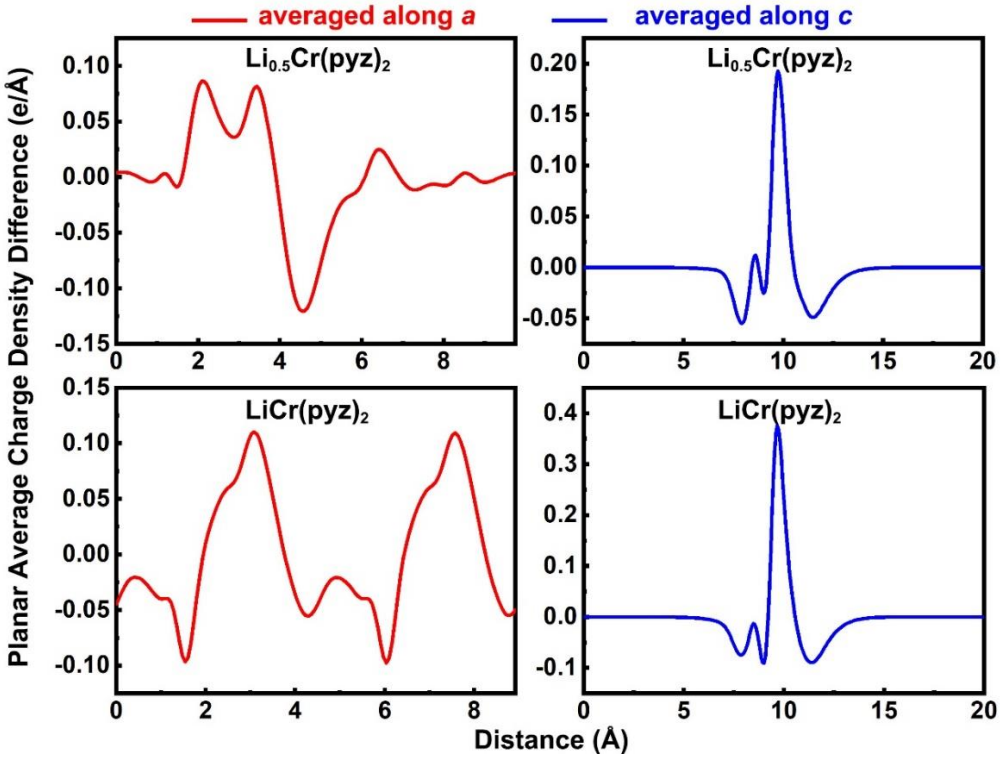

Figure S2. The planar average charge density difference of $Li_{0.5}Cr(pyz)_2$ and $LiCr(pyz)_2$ along the in-plane (lattice *a* direction) and out-of-plane (lattice *c* direction) directions. The charge

density difference ρ_{diff} is calculated by $\rho_{diff} = \rho_{Li\text{-}MOF} - \rho_{Li} - \rho_{MOF}$, where the $\rho_{Li\text{-}MOF}$, ρ_{Li}, and ρ_{MOF} represent the charge density of Li decorated $Cr(pyz)_2$, Li atoms, and $Cr(pyz)_2$, respectively. It can be seen that the charge density difference along the in-plane direction is much more asymmetric than the out-of-plane one. This suggests the Li adsorption induces a more predominant charge density redistribution in the in-plane direction rather than the out-of-plane direction, which then leads to the much larger in-plane electric polarization.

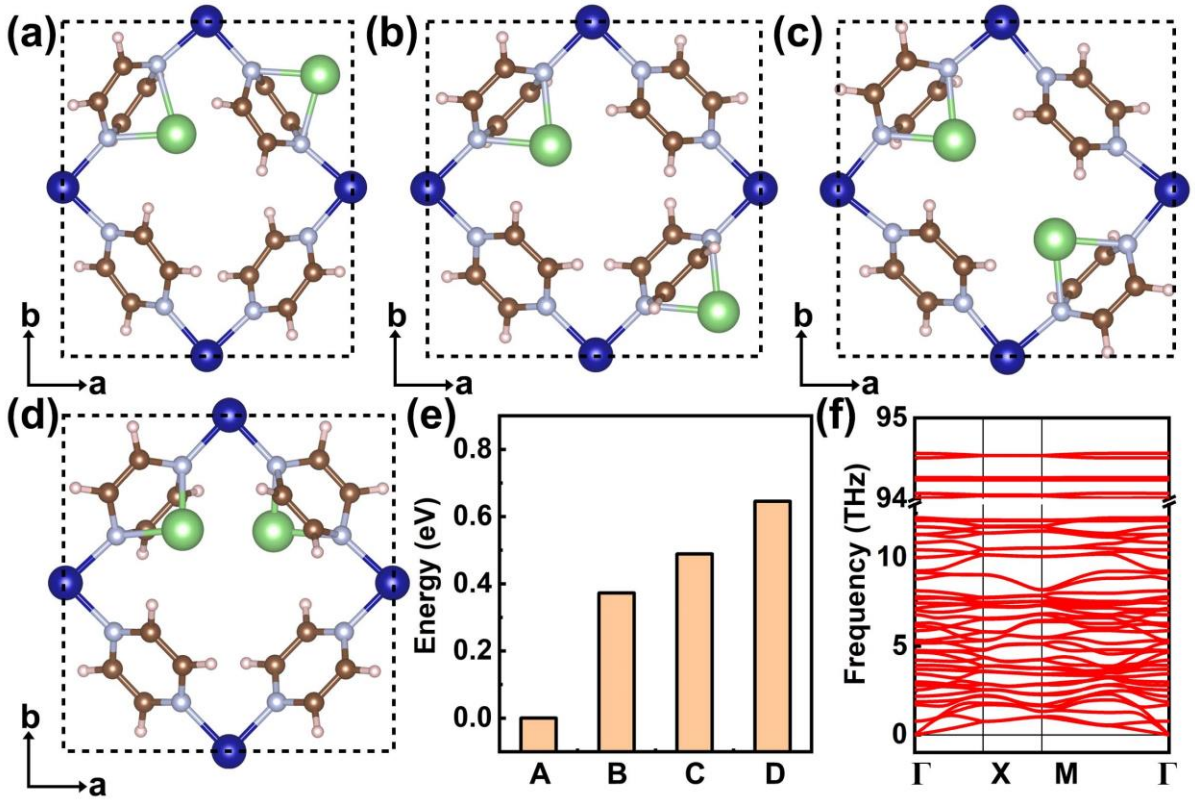

Figure S3. (a)-(d) $LiCr(pyz)_2$ in different Li-pyrazine patterns. (e) Energy comparison of $LiCr(pyz)_2$ in different Li-pyrazine patterns. (f) Phonon spectra of $LiCr(pyz)_2$ in configuration A.

Note S1.

For 2D $Li_{0.5}Cr(pyz)_2$, the direction of P_{out} is dependent on that of P_{in}, thus we write the local P_i as [1, 1],[1, -1],[-1, 1], and [-1, -1], and the coupling parameters matrix $\boldsymbol{J}$ can be written in the following form:

$$\boldsymbol{J} = \begin{bmatrix} J^{xx} & J^{xy} \\ J^{yx} & J^{yy} \end{bmatrix}$$

Considering the interaction between P_i ([a, b]) and P_j ([c, d]), $P_i \boldsymbol{J} P_j$ shall equal to $P_j \boldsymbol{J} P_i$ because they are the same pair of interaction. Then we can get the following equation:

$$\mathrm{ac}J^{xx} + bcJ^{yx} + adJ^{xy} + bdJ^{yy} = \mathrm{ac}J^{xx} + adJ^{yx} + bcJ^{xy} + bdJ^{yy}$$

Hence, J^{yx} equals to J^{xy} and the $\boldsymbol{J}$ is a symmetric matrix. Similarly, we can find the $\boldsymbol{J_a}$ and $\boldsymbol{J_b}$ for $LiCr(pyz)_2$ are also symmetric. The energy of the two polarized phases as shown in Figure S4a and S4b can be expressed as $E_0 + 4J^{xx} - 4J^{xy} - 4J^{yx} + 4J^{yy}$ and $E_0 + 4J^{xx} + 4J^{xy} + 4J^{yx} + 4J^{yy}$, respectively. Because the two polarized phases are equivalent in energy, we can then get $J^{xy} = J^{yx} = 0$. Three configurations as shown in Figure S5a-c are constructed to extract the remaining unknown variables. The lattice parameters are fixed and the atomic positions are optimized to obtain the total energies. Using the Hamiltonian for 2D $Li_{0.5}Cr(pyz)_2$ and the DFT calculated energy, we can get the following equation:

$$\begin{bmatrix} 0 & 4 & 1 \\ 4 & 0 & 1 \\ 4 & 4 & 1 \end{bmatrix} \begin{bmatrix} J^{xx} \\ J^{yy} \\ E_0 \end{bmatrix} = \begin{bmatrix} E_1 \\ E_2 \\ E_3 \end{bmatrix}$$

where the E_1, E_2, and E_3 are the DFT calculated energy of the configurations shown in Figure S5a-c, respectively. Solving this equation we can then get the coupling parameters for 2D $Li_{0.5}Cr(pyz)_2$, which are summarized in Table S1.

Table S1. The dipole-dipole coupling parameters of 2D $Li_{0.5}Cr(pyz)_2$ (in meV).

J^{xx}	$J^{xy} = J^{yx}$	J^{yy}
-11	0	-23

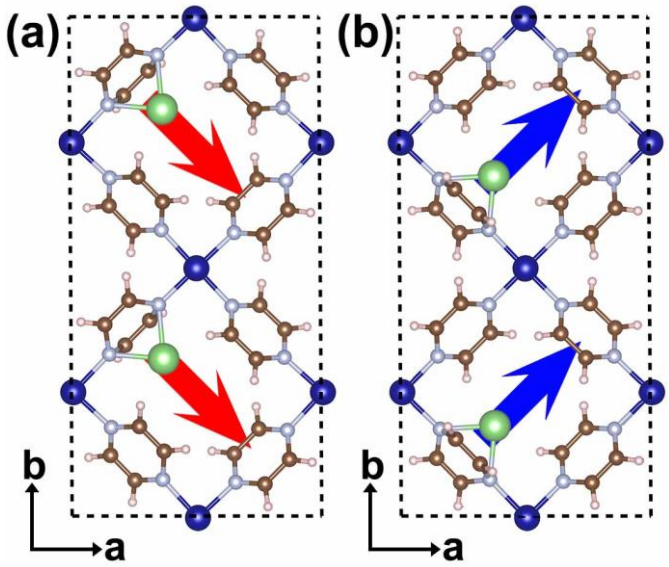

Figure S4. Two degenerate polarized phases of 2D $Li_{0.5}Cr(pyz)_2$. The arrows represent the polarization vectors. The red and blue colour marks the positive and negative out-of-plane polarization, respectively.

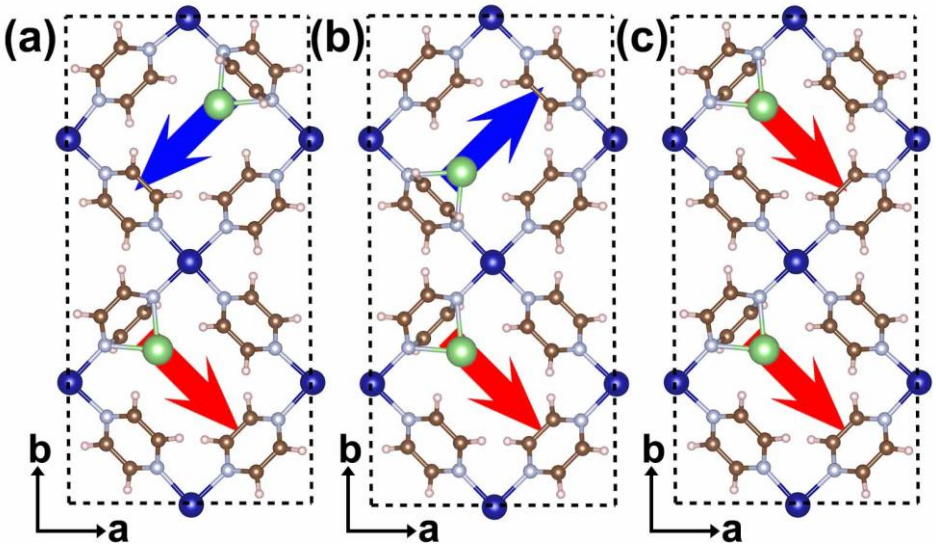

Figure S5. (a)-(c) The configurations used to extract the dipole-dipole coupling parameters of 2D $Li_{0.5}Cr(pyz)_2$ with the local polarization marked by arrows.

For 2D LiCr(pyz)$_2$, the direction of P_{out} is independent of that of P_{in}, thus all the possible local P_i can be written as [1, 0, 1], [1, 0, -1], [-1, 0, 1], [-1, 0, -1], [0, 1, 1], [0, 1, -1], [0, -1, 1], and [0, -1, -1], and the $\boldsymbol{J_a}$ and $\boldsymbol{J_b}$ take the following forms:

$$\boldsymbol{J_a} = \begin{bmatrix} J_a^{xx} & J_a^{xy} & J_a^{xz} \\ J_a^{yx} & J_a^{yy} & J_a^{yz} \\ J_a^{zx} & J_a^{zy} & J_a^{zz} \end{bmatrix} \text{ and } \boldsymbol{J_b} = \begin{bmatrix} J_b^{xx} & J_b^{xy} & J_b^{xz} \\ J_b^{yx} & J_b^{yy} & J_b^{yz} \\ J_b^{zx} & J_b^{zy} & J_b^{zz} \end{bmatrix}$$

where $\boldsymbol{J_a} = \boldsymbol{J_a^T}$ and $\boldsymbol{J_b} = \boldsymbol{J_b^T}$. Considering the two polarized phases of 2D LiCr(pyz)$_2$ shown in Figures S6a and S6b, their energy can be written as $E_0 + 4\mathrm{K} + 4J_a^{xx} + 4J_a^{xz} + 4J_a^{zx} + 4J_a^{zz} + 4J_b^{xx} + 4J_b^{xz} + 4J_b^{zx} + 4J_b^{zz}$ and $E_0 + 4\mathrm{K} + 4J_a^{xx} - 4J_a^{xz} - 4J_a^{zx} + 4J_a^{zz} + 4J_b^{xx} - 4J_b^{xz} - 4J_b^{zx} + 4J_b^{zz}$, respectively. Because these two polarized states are degenerate in energy, thus we get $J_a^{xz} = -J_b^{xz}$. Similarly, using the energy of the two polarized phases as shown in Figures S6c and S6d, we can get $J_a^{yz} = -J_b^{yz}$. To get all the coupling parameters, we constructed 12 configurations as shown in Figure S7 and by mapping their energy we get the following equation:

$$\begin{bmatrix} 4 & 0 & 0 & 0 & 0 & 4 & 4 & 0 & 0 & 4 & 1 & 4 \\ 0 & 0 & 0 & 4 & 0 & 4 & 0 & 0 & 4 & 4 & 1 & 0 \\ 0 & 4 & -8 & 0 & 8 & -4 & 2 & 0 & 2 & 4 & 1 & 2 \\ -4 & 0 & -16 & 0 & 0 & -4 & 4 & 0 & 0 & 4 & 1 & 4 \\ 0 & 0 & 0 & -4 & -16 & -4 & 0 & 0 & 4 & 4 & 1 & 0 \\ 4 & 0 & 0 & 0 & 0 & -4 & 4 & 0 & 0 & 4 & 1 & 4 \\ -4 & 0 & 0 & 0 & 0 & 4 & 4 & 0 & 0 & 4 & 1 & 4 \\ 2 & 0 & 8 & 2 & -8 & 4 & 0 & 4 & 0 & -4 & 1 & 2 \\ 0 & 0 & 0 & 4 & 16 & 4 & 0 & 0 & -4 & -4 & 1 & 0 \\ 4 & 0 & 0 & 0 & 0 & 4 & 4 & 0 & 0 & -4 & 1 & 4 \\ 4 & 0 & 0 & 0 & 0 & 4 & -4 & 0 & 0 & 4 & 1 & 4 \\ 2 & 0 & 0 & 2 & 0 & 4 & 0 & 4 & 0 & 4 & 1 & 2 \end{bmatrix} \begin{bmatrix} J_a^{xx} \\ J_a^{xy} \\ J_a^{xz} \\ J_a^{yy} \\ J_a^{yz} \\ J_a^{zz} \\ J_b^{xx} \\ J_b^{xy} \\ J_b^{yy} \\ J_b^{zz} \\ E_0 \\ K \end{bmatrix} = \begin{bmatrix} E_1 \\ E_2 \\ E_3 \\ E_4 \\ E_5 \\ E_6 \\ E_7 \\ E_8 \\ E_9 \\ E_{10} \\ E_{11} \\ E_{12} \end{bmatrix}$$

where the E_1-E_{12} are the DFT calculated energy of the configurations shown in Figure S7a-S7l, respectively. Solving this equation, we then get all the independent coupling parameters as summarized in Table S2.

Table S2. The independent dipole-dipole coupling parameters of 2D $LiCr(pyz)_2$ (in meV).

J_a^{xx}	J_a^{xy}	J_a^{xz}	J_a^{yy}	J_a^{yz}	J_a^{zz}	J_b^{xx}	J_b^{xy}	J_b^{yy}	J_b^{zz}	K
-162	-52	14	14	35	-116	-5	24	23	-34	-178

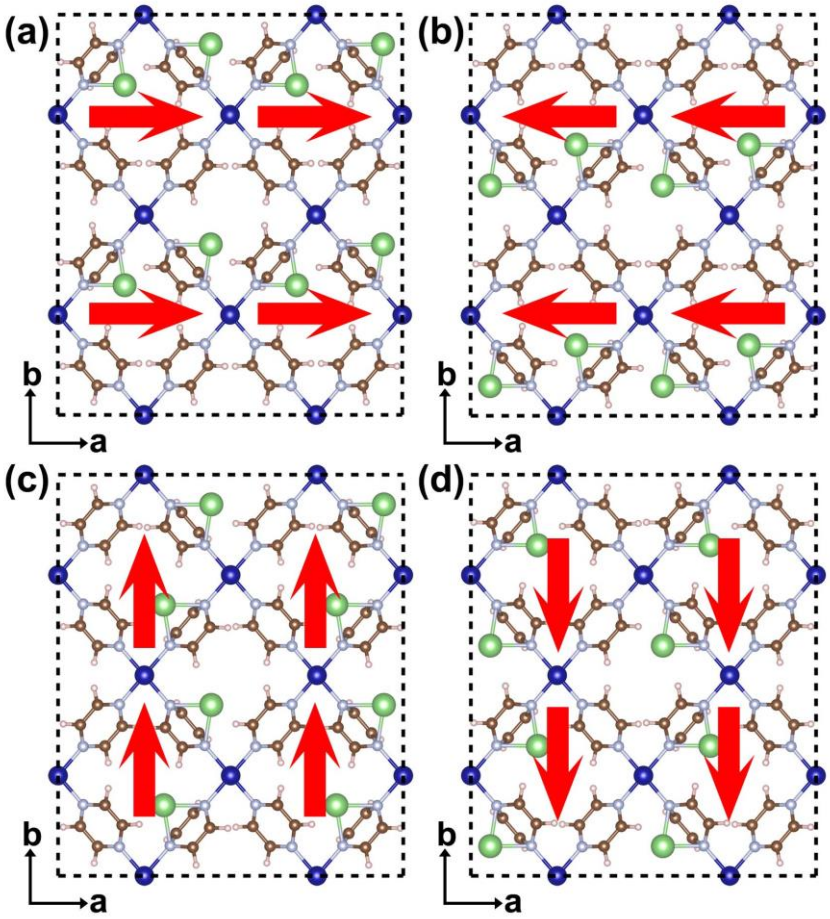

Figure S6. (a)-(d) Four polarized phases of 2D $LiCr(pyz)_2$ with the local polarization marked by arrows. The degenerate configurations (a) and (b) are not equivalent to the degenerate configurations (c) and (d), because the lattice parameters $a < b$ are fixed when extracting the coupling parameters.

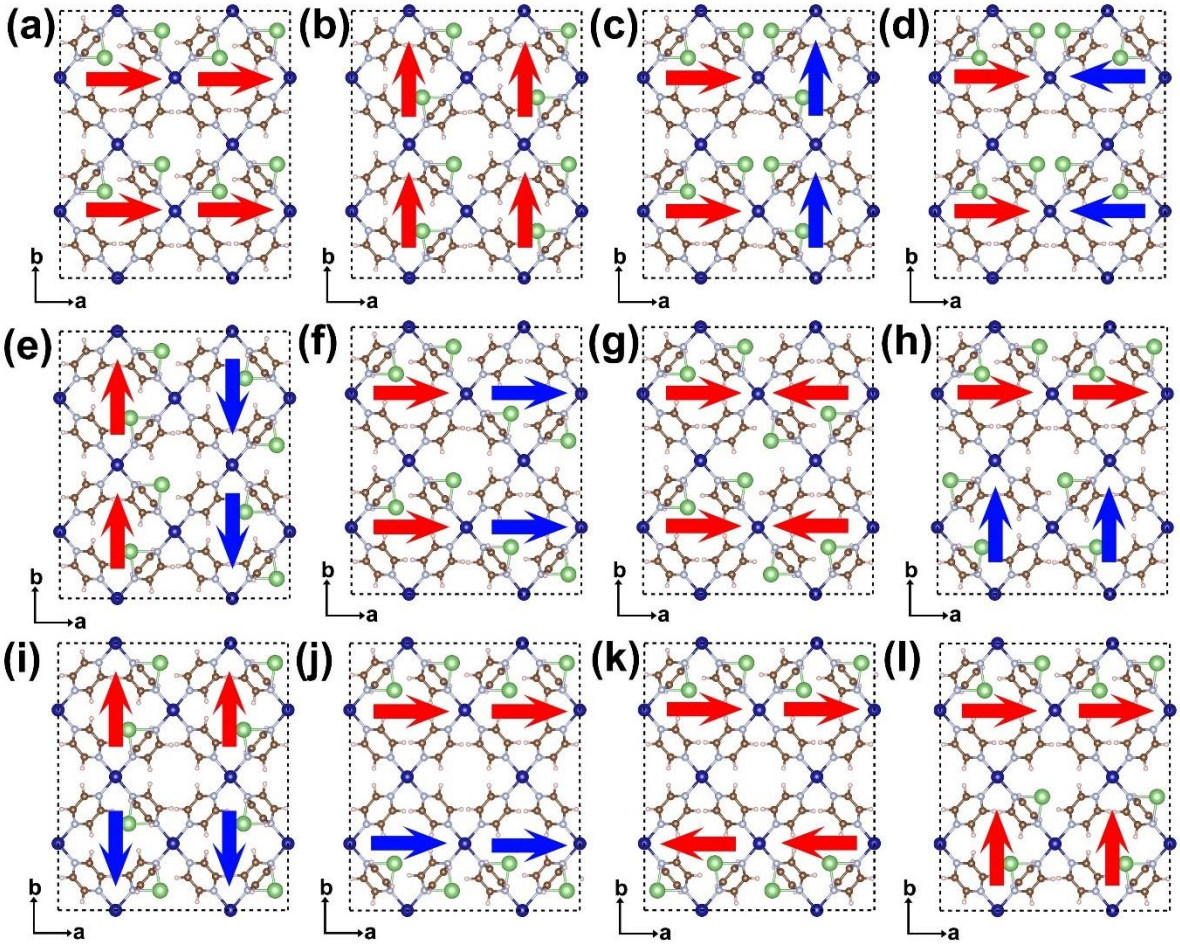

Figure S7 (a)-(l) The configurations used to extract the dipole-dipole coupling parameters of 2D $LiCr(pyz)_2$ with the local polarization marked by arrows.

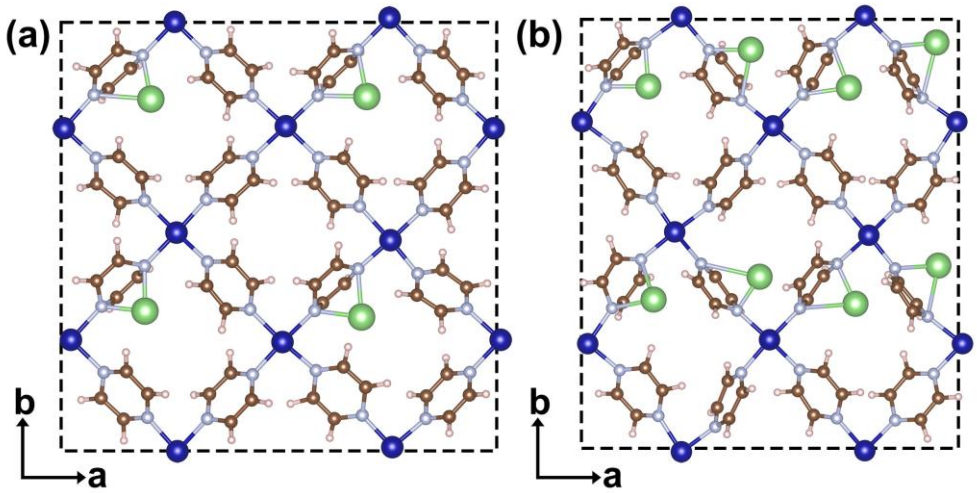

Figure S8. (a) and (b) The atomic structures of 2D $Li_{0.5}Cr(pyz)_2$ and $LiCr(pyz)_2$ at the end of AIMD simulations performed at 200 K and 250 K, respectively.

To explore the possibility of adsorption-induced curling of the 2D MOF, we calculated the energy of $LiCr(pyz)_2$ nanoribbons with different curvatures and compared the energy with the flat one, as shown in the Figure S9. We kept the periodic boundary condition of $LiCr(pyz)_2$ in either direction *a* or *b* while keeping the other direction open. The nanoribbons were then bent along the open boundary direction with different curvatures. The width of $LiCr(pyz)_2$ nanoribbons is four-unit-cells long and atoms at the edge were fixed during the optimization. Because the width of the nanoribbons is fixed, a smaller θ (as shown in the inset of Figure S9) represents a smaller curvature and vice versa. As we can see from Figure S9, the energy of $LiCr(pyz)_2$ nanoribbon increases as the curvature becomes large, indicating the instability of the bent nanoribbons. Hence, the Li decorated $Cr(pyz)_2$ may keep the planar structures.

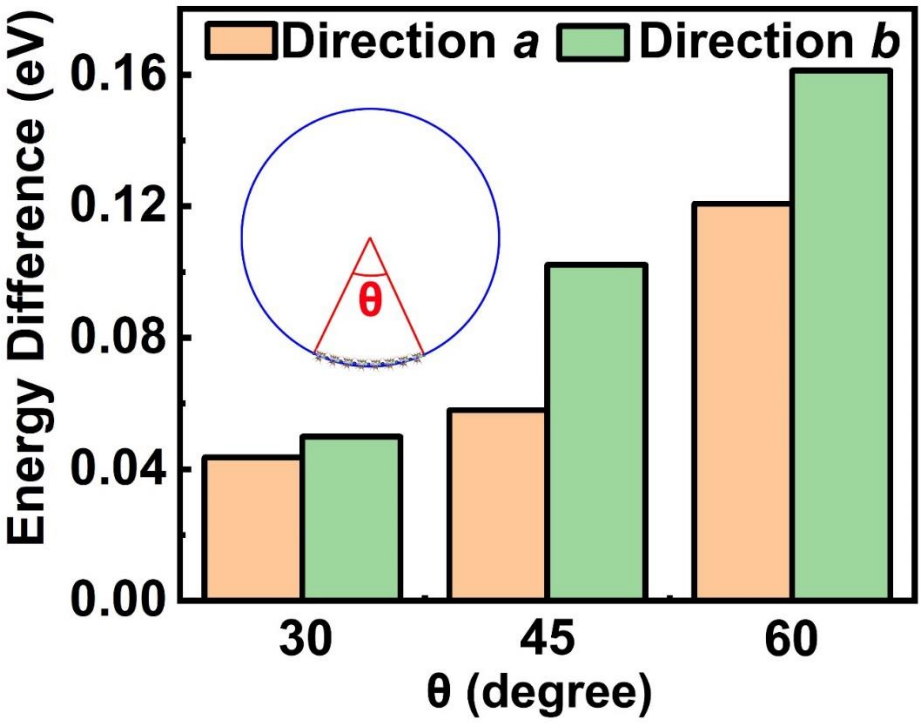

Figure S9. The energy difference between bent (along both lattice a and b directions) and flat nanoribbon $LiCr(pyz)_2$. The insets show the definition of θ. The arc length corresponding to θ equals to the width of the nanoribbon.

Note S2.

We compared the energy of $Li_{0.5}Cr(pyz)_2$ in 1×2×1 supercells with different Li patterns, as shown in Figure S10. Configuration A is the one reported in our manuscript with the Li atoms uniformly distributed in the MOF, while configuration B is the one with Li atoms occupying only half of the supercell. We found that configuration B is lower in energy by around 0.07 eV per unit formula than configuration A. It can be seen that the Li atoms favour a linear arrangement along the lattice a direction, which is similar to that of $LiCr(pyz)_2$. Four energetically degenerate polarized states can be found for $Li_{0.5}Cr(pyz)_2$ in configuration B, as shown in Figure S11, of which the P_{in} and P_{out} is 2.64 and 0.26 μC/cm^2, respectively.

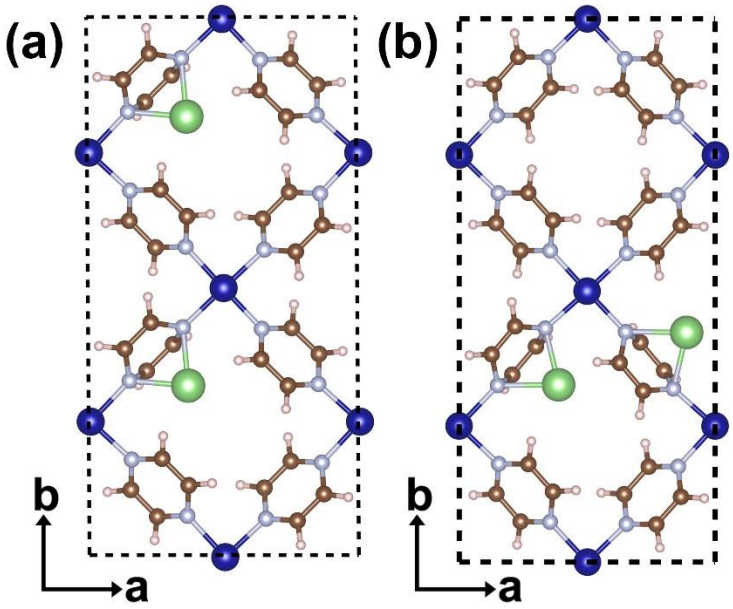

Figure S10. (a) and (b) The 1×2×1 supercells of $Li_{0.5}Cr(pyz)_2$ in configuration A and B respectively.

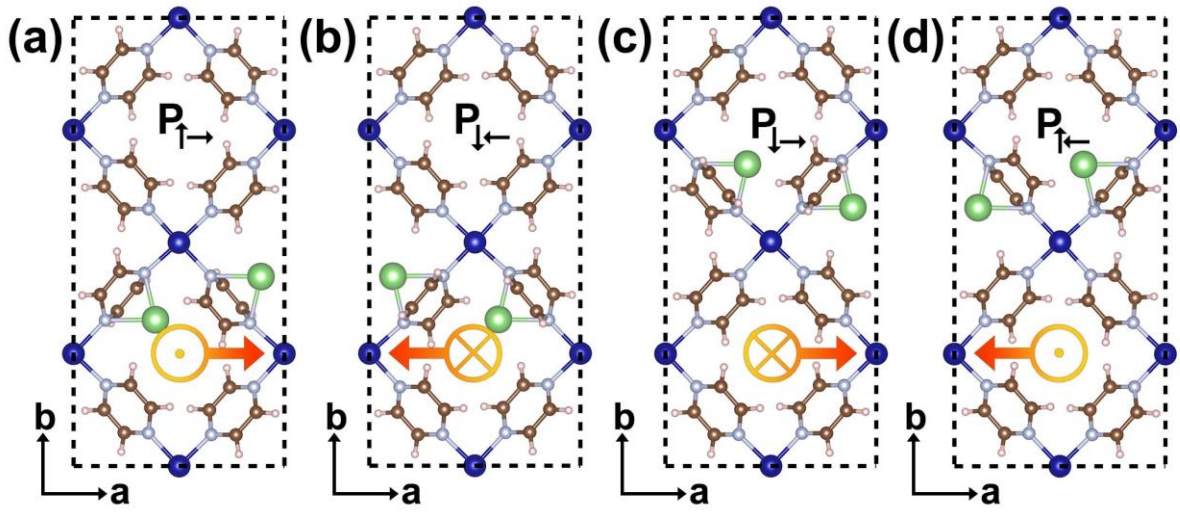

Figure S11. The four degenerate polarized phases of $Li_{0.5}Cr(pyz)_2$ in configuration B.

The transition between $P_{\uparrow\rightarrow}$ ($P_{\downarrow\rightarrow}$) and $P_{\downarrow\leftarrow}$ ($P_{\uparrow\leftarrow}$) states reverses both P_{in} and P_{out} as shown in Figure S12a, which can proceed through the Li migration within the pore with an energy barrier of 0.18 eV/Li atom, close to that of type I transition of $LiCr(pyz)_2$ (0.15 eV/Li atom). However, the transition between $P_{\uparrow\rightarrow}$/ $P_{\downarrow\leftarrow}$ states and $P_{\uparrow\leftarrow}$/$P_{\downarrow\rightarrow}$ states which only switches the P_{in} or P_{out} requires the Li migration between different pores, which is unlikely to happen because the long migration distance. This is supported by the tracked trajectory of Li movements during AIMD simulations as shown in Figure S13, where the Li migration is found confined within the pore. Hence, the ferroelectricity of $Li_{0.5}Cr(pyz)_2$ in configuration B is two-fold degenerate, which falls outside the scope of our investigation for high-degenerate ferroelectricity.

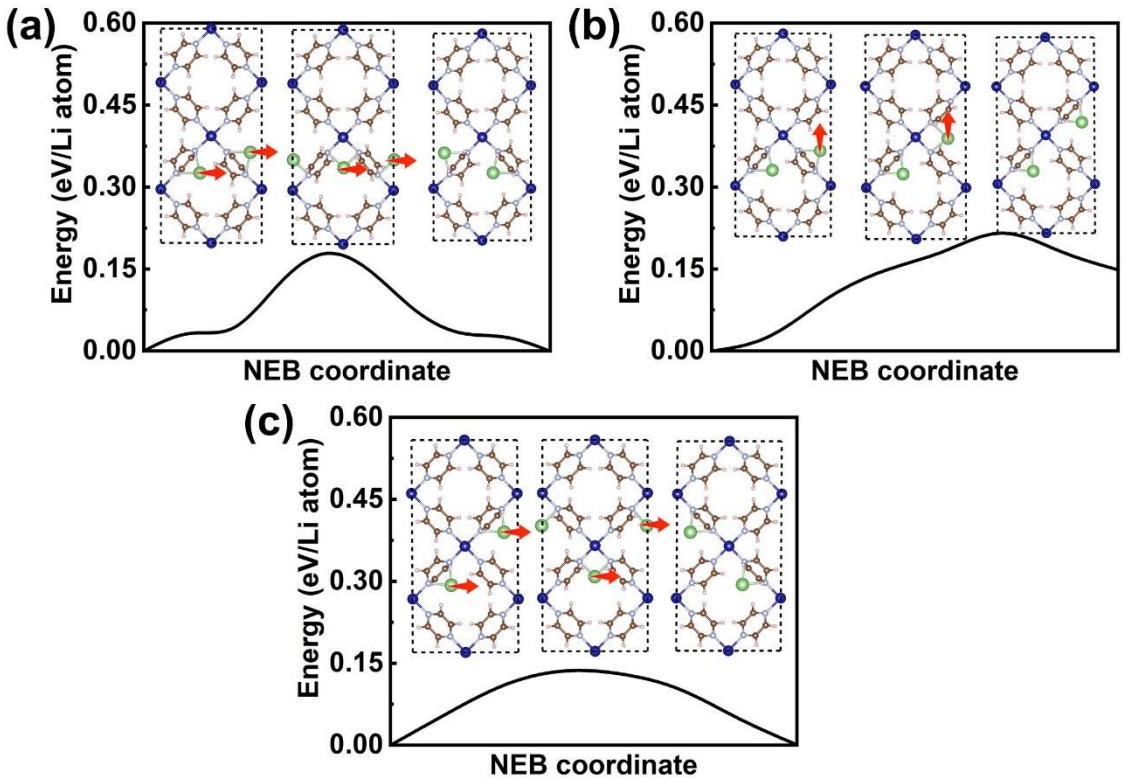

Figure S12. (a) The FE switching barrier of $Li_{0.5}Cr(pyz)_2$ in configuration B. (b) The transition barrier from configuration B to configuration C. (c) The FE switching barrier of $Li_{0.5}Cr(pyz)_2$ in configuration C.

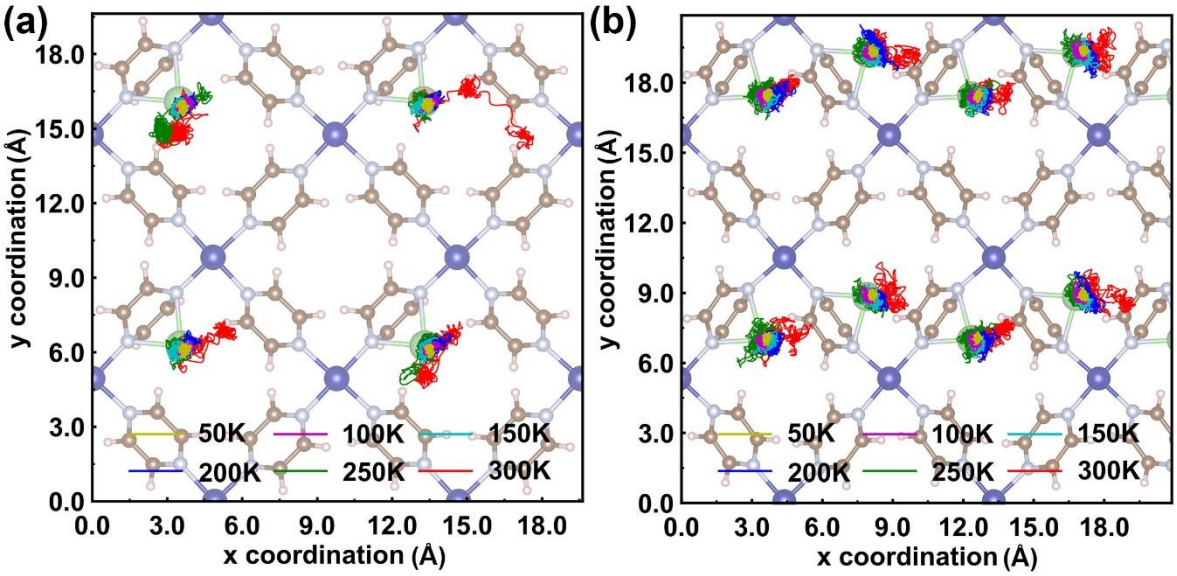

Figure S13. (a) and (b) The Li trajectory during the AIMD simulations for $Li_{0.5}Cr(pyz)_2$ (in configuration A) and $LiCr(pyz)_2$ in different temperature, respectively.

Interestingly, we found that $Li_{0.5}Cr(pyz)_2$ in configuration B can be transited to configuration C through Li migration within the pores, where the Li-pyrazine in different pores point to the same in-plane direction, as shown in Figure S14. The transition barrier from configuration B to C is calculated to be around 0.22 eV/Li atom (see Figure S12b), suggesting the transition can proceed at a moderate energy cost. Moreover, the reversing transition from configuration C to B requires an energy barrier of 0.07 eV/Li atom, indicating once configuration C is obtained, it will not spontaneously switch back to configuration B.

The energy of configuration C is only slightly higher than configuration A (~3meV) and they share similar ferroelectric behavior. We can still find four energetically degenerate polarized states (similar to configuration A) as shown in Figure S14. The P_{in} is calculated to be around 5.55 μC/cm^2 and the overall P_{out} is zero because the two Li-pyrazine rings point upward and downward respectively, whose P_{out} cancels each other out. In this case, the four degenerate polarized phases can be switched between each other through Li migration within the pores. The transition vertically switching the P_{in} is considered, whose transition barrier is calculated to be 0.14 eV/Li atom (see Figure 12c). For comparison, the P_{in} and energy barrier for a similar transition pathway for configuration A are 5.33 μC/cm^2 and 0.12 eV/Li atom, respectively.

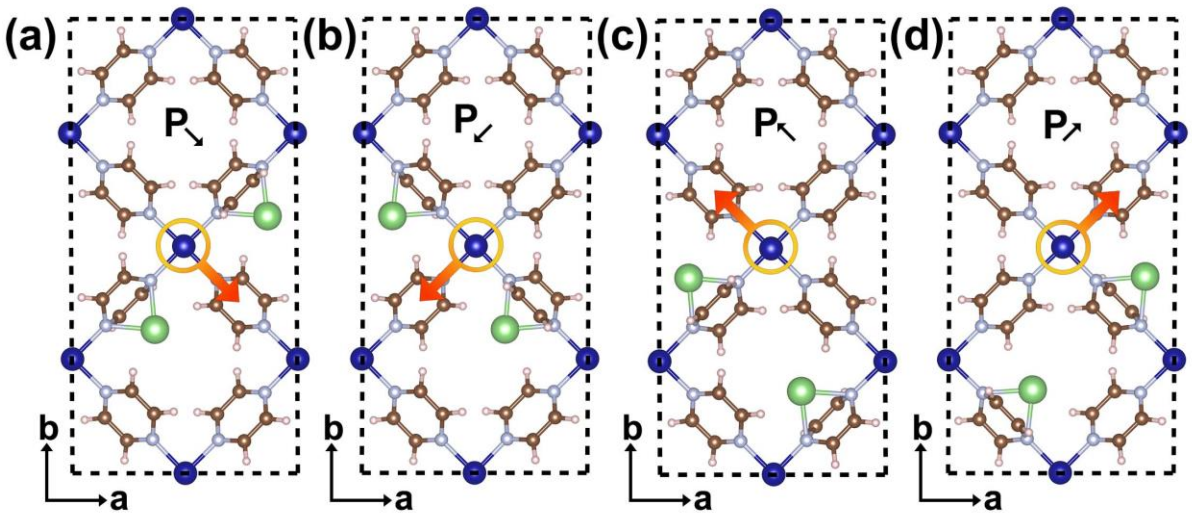

Figure S14. The four degenerate polarized phases of $Li_{0.5}Cr(pyz)_2$ in configuration C.

In short, the Li occupation of different pores can change the ground states of $Li_{0.5}Cr(pyz)_2$. Indeed, if the supercell becomes even larger, there will be infinite configurations that cannot be fully addressed by calculations. Fortunately, the highly degenerate polarity at a single Li-occupied pore site is always valid because this is solely associated with the symmetry of the host materials. If we align the Li-pyrazine in different pores to the same direction (similar to configuration C) at some energy cost, we may still achieve the high degenerate ferroelectricity as described in our work.

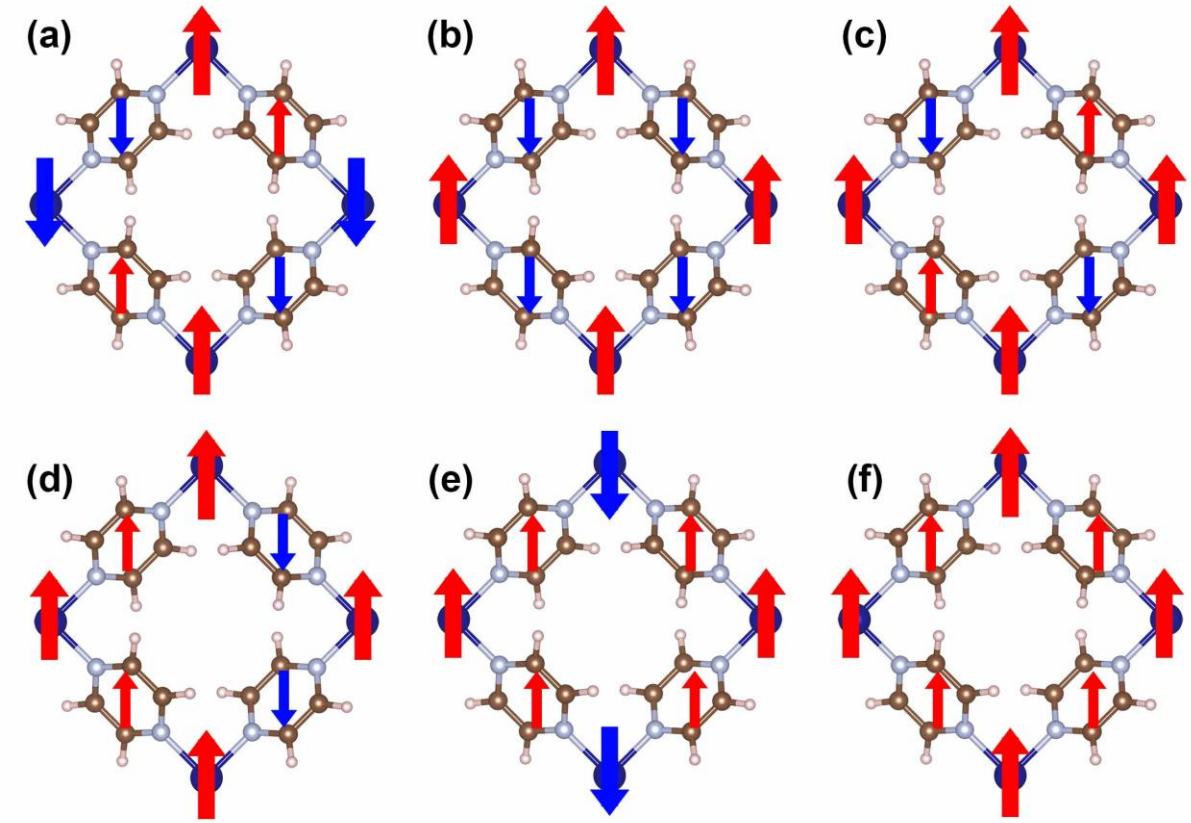

Figure S15. (a)-(f) The AFM, FiM1, FiM2, FiM3, FIM4, and FM magnetic configuration in pristine 2D $Cr(pyz)_2$, respectively. The red and blue arrows represent the spin-up and spin-down magnetic moments.

Table S3. Energy (in eV) of 2D $Cr(pyz)_2$, $Li_{0.5}Cr(pyz)_2$, and $LiCr(pyz)_2$ in different magnetic configurations and the MAE values (in μeV/Cr).

	AFM	FiM1	FiM2	FiM3	FiM4	FM	MAE
$Cr(pyz)_2$	0.63	0.00	0.70	0.72	0.73	1.54	237
$Li_{0.5}Cr(pyz)_2$	0.47	0.00	0.69	0.34	0.52	1.11	241
$LiCr(pyz)_2$	0.30	0.00	0.32	0.32	0.34	0.72	254

Table S4. The magnetic moments (in μB) of Cr atom, pyrazine and Li-pyrazine for pristine and Li-decorated 2D $Cr(pyz)_2$.

	Cr	Pyrazine	Li-pyrazine
$Cr(pyz)_2$	3.59	-0.59	-
$Li_{0.5}Cr(pyz)_2$	3.62	-0.59	-0.03
$LiCr(pyz)_2$	3.64	-0.59	-0.03

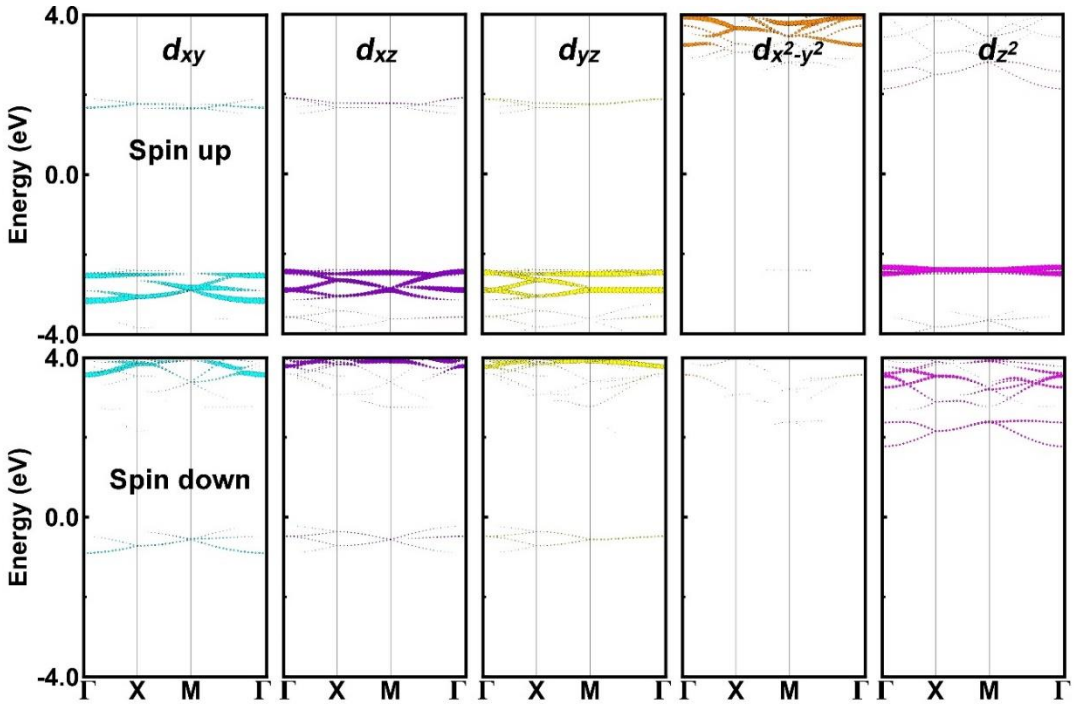

Figure S16. The orbital decomposed band structures for Cr in pristine $Cr(pyz)_2$ calculated by HSE06 functional.

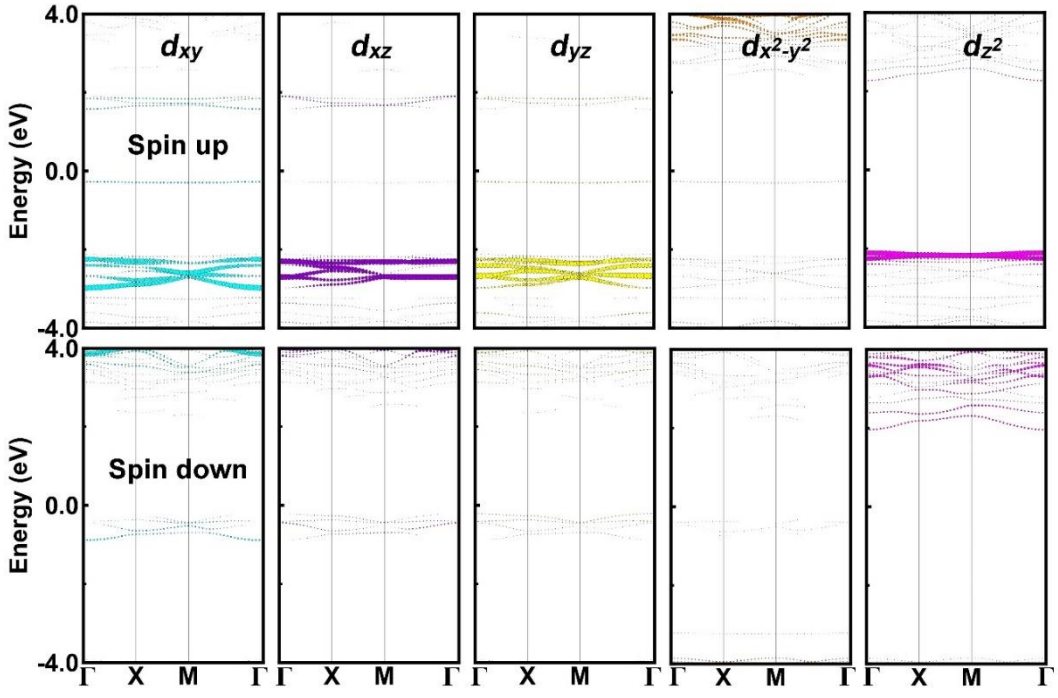

Figure S17. The orbital decomposed band structures for Cr in $Li_{0.5}Cr(pyz)_2$ calculated by HSE06 functional.

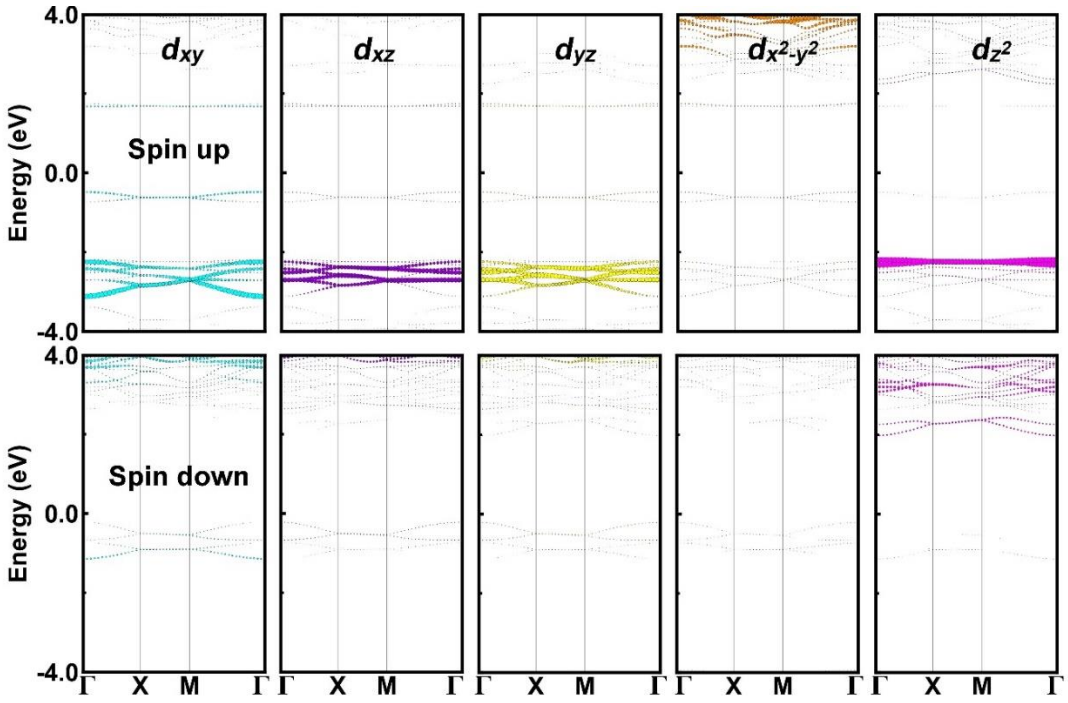

Figure S18. The orbital decomposed band structures for Cr in $LiCr(pyz)_2$ calculated by HSE06 functional.

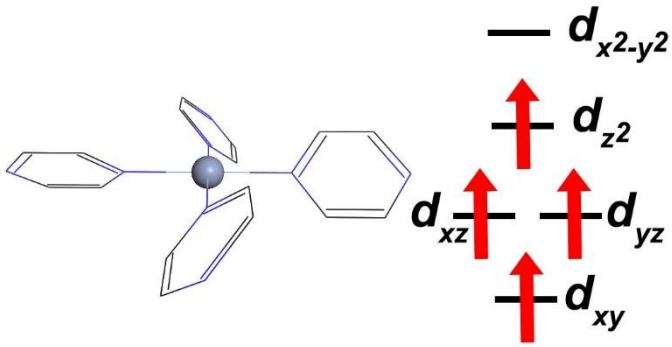

Figure S19. The spin configuration of Cr in both the pristine $Cr(pyz)_2$ and its Li-decorated variants. The red arrows mark the spin-up electrons.

Note S3:

The g-C_3N_4 and C_2N monolayers are both experimentally fabricated and display uniform triangular and hexagonal pores, respectively, as shown in Figure S20 and S22. We choose P

and Ru dopants for g-C_3N_4 and C_2N monolayers respectively, because the possibility of P (Ru) surface decoration to g-C_3N_4 (C_2N) monolayer has been experimentally demonstrated.[15, 16] Firstly, we focus on the P decorated g-C_3N_4. Three binding sites in the pore have been considered and it is found the P atom tend to bind with the two N atoms at the corner of the pore and forming a flat atomic structure. Due to the three-fold rotation symmetry, P decorated g-C_3N_4 with P atom occupying any of the three corners will be equivalent, leading to the three-fold degenerate polarized phases as shown in Figure S21a-c. We mark them as $P_{\nearrow}$, $P_{\nwarrow}$, and $P_{\downarrow}$, where the arrow in the subscript represents the direction of polarization. As the structure is flat, only in-plane polarization is observed which is calculated to be 1.49 μC/cm^2 and its direction is shown in Figure S21a-c. The FE switching is then studied by cNEB calculations, as shown in Figure S21d. It is found the P atom moves to another corner by crossing an intermediate state where the P atom binds to two N atoms at the central part of one pore edge, given a transition barrier of 0.45 eV/P atom. For Ru decorated C_2N, the Ru atom also binds with two N atoms at the pore edge (Figure S22) and the six-fold rotation symmetry of 2D C_2N give rises to six-fold degenerate polarized states as shown in Figure S23 ($P_{\nearrow}$, $P_{\uparrow}$, $P_{\nwarrow}$, $P_{\swarrow}$, $P_{\downarrow}$, and $P_{\searrow}$). The atomic structure is also flat and the in-plane polarization is calculated to be 3.42 μC/cm^2. The transition between $P_{\nearrow}$ state to $P_{\uparrow}$ state with shortest Ru migration distance is explored and shown in Figure S23g. The transition goes through an intermediate state where Ru atom binds to one N atom at the pore edge, with a transition barrier of 0.06 eV/Ru atom.

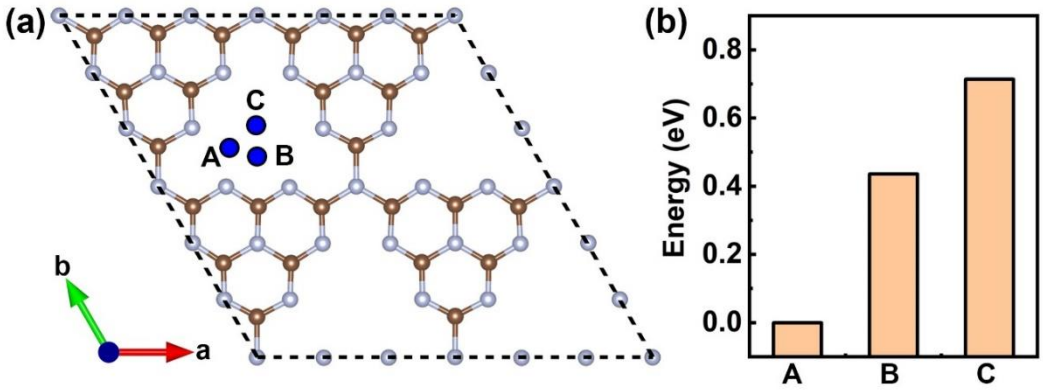

Figure S20. (a) Adsorption sites of P atoms in a 2×2×1 supercell of 2D g-C_3N_4. (b) The energy of P decorated g-C_3N_4 with different P positions. The energy of configuration A is set to zero for comparison.

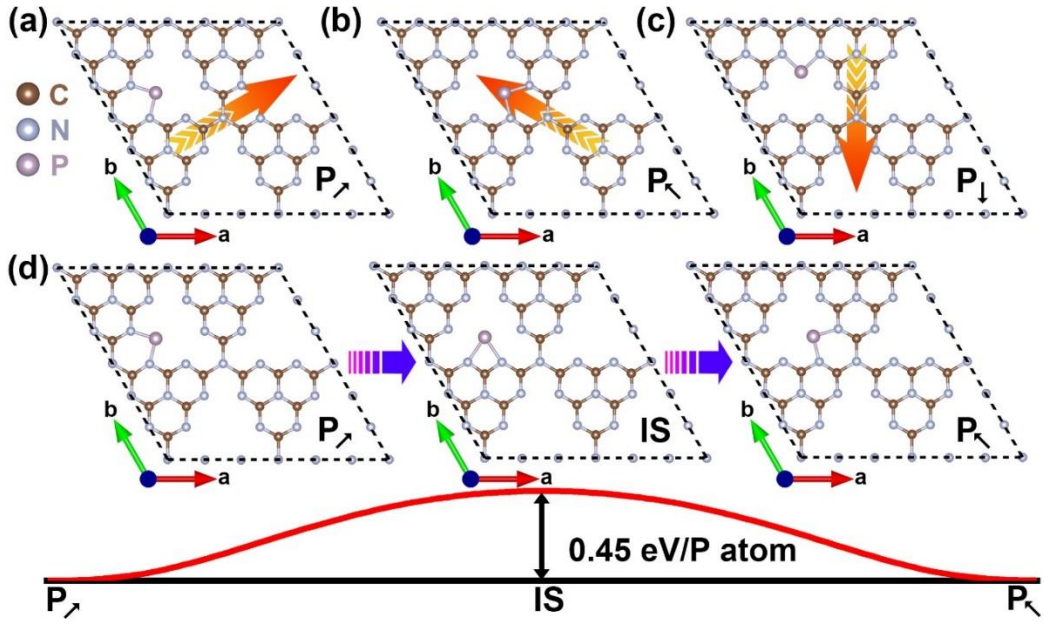

Figure S21. (a)-(c) The three equivalent polarized configuration of P decorated g-C_3N_4. The arrows mark the direction of spontaneous polarization. (d) The energy profile of the FE transition from P↗ state to P↖ state through an intermediate state (IS).

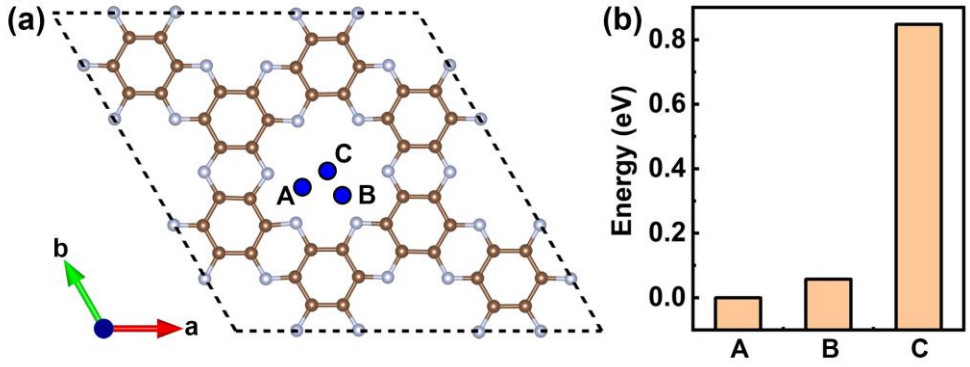

Figure S22. (a) Adsorption sites of the Ru atom in a 2×2×1 supercell of 2D C_2N. (b) The energy of Ru decorated C_2N with different Ru positions. The energy of configuration A is set to zero for comparison.

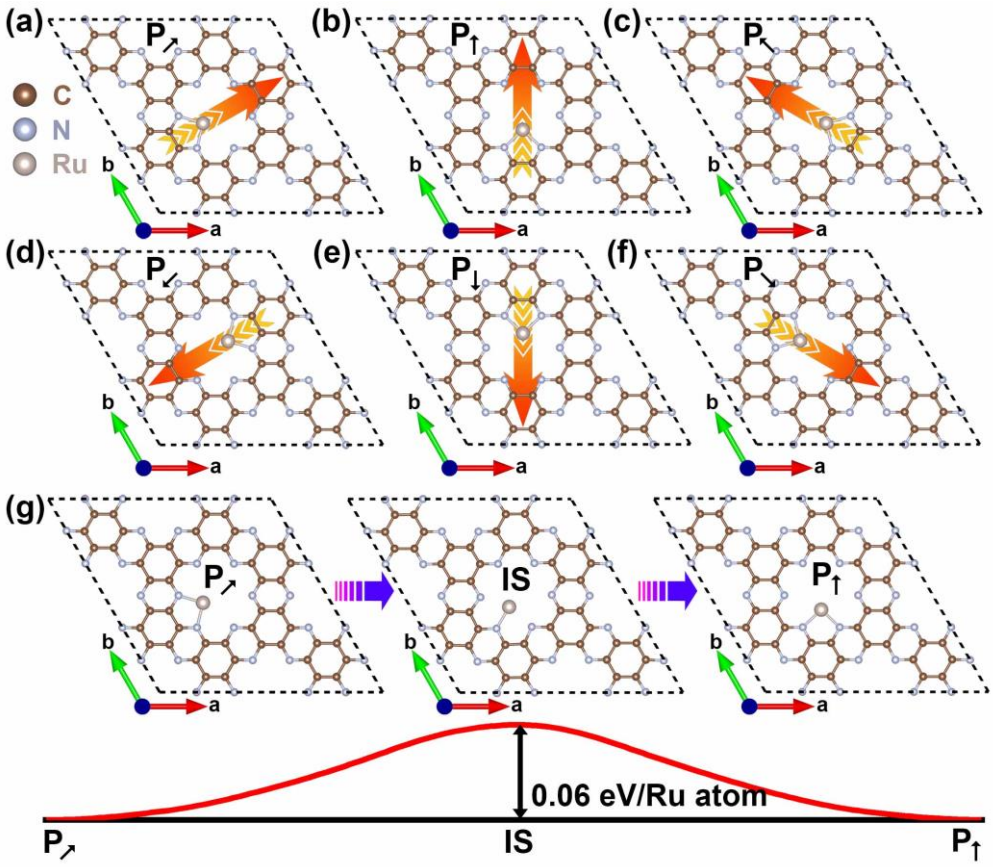

Figure S23. (a)-(f) The six equivalent polarized configuration of Ru decorated C_2N. The arrows mark the direction of spontaneous polarization. (g) The energy profile of the FE transition from $P_{\nearrow}$ state to $P_{\uparrow}$ state through an intermediate state (IS).

References

1. G. Kresse; J. Furthmüller, Efficiency of Ab-Initio Total Energy Calculations for Metals and Semiconductors Using a Plane-Wave Basis Set. *Computational Materials Science* **1996,** *6* (1), 15-50.
2. G. Kresse; J. Furthmüller, Efficient Iterative Schemes for Ab Initio Total-Energy Calculations Using a Plane-Wave Basis Set. *Physical Review B* **1996,** *54* (16), 11169-11186.
3. G. Kresse; J. Hafner, Ab Initio Molecular-Dynamics Simulation of the Liquid-Metal-Amorphous-Semiconductor Transition in Germanium. *Physical Review B* **1994,** *49* (20), 14251-14269.
4. G. Kresse; D. Joubert, From Ultrasoft Pseudopotentials to the Projector Augmented-Wave Method. *Physical Review B* **1999,** *59* (3), 1758-1775.
5. J. P. Perdew; M. Ernzerhof; K. Burke, Rationale for Mixing Exact Exchange with Density Functional Approximations. *Journal of Chemical Physics* **1996,** *105* (22), 9982-9985.
6. John P Perdew; Kieron Burke; Matthias Ernzerhof, Generalized Gradient Approximation Made Simple. *Physical Review Letters* **1996,** *77* (18), 3865.
7. S. Grimme, Semiempirical GGA-Type Density Functional Constructed with A Long-Range Dispersion Correction. *Journal of Computational Chemistry* **2006,** *27* (15), 1787-1799.
8. Haifeng Lv; Xiangyang Li; Daoxiong Wu; Ying Liu; Xingxing Li; Xiaojun Wu; Jinlong Yang, Enhanced Curie Temperature of Two-Dimensional Cr(II) Aromatic Heterocyclic Metal–Organic Framework Magnets via Strengthened Orbital Hybridization. *Nano Letters* **2022,** *22* (4), 1573-1579.
9. Aliaksandr V. Krukau; Oleg A. Vydrov; Artur F. Izmaylov; Gustavo E. Scuseria, Influence of the Exchange Screening Parameter on the Performance of Screened Hybrid Functionals. *The Journal of Chemical Physics* **2006,** *125* (22), 224106.
10. Gregory Mills; Hannes Jónsson; Gregory K. Schenter, Reversible Work Transition State Theory: Application to Dissociative Adsorption of Hydrogen. *Surface Science* **1995,** *324* (2), 305-337.
11. D. J. Evans, Computer ‘‘Experiment’’ for Nonlinear Thermodynamics of Couette Flow. *The Journal of Chemical Physics* **1983,** *78* (6), 3297-3302.
12. Bohayra Mortazavi; Ivan S. Novikov; Evgeny V. Podryabinkin; Stephan Roche; Timon Rabczuk; Alexander V. Shapeev; Xiaoying Zhuang, Exploring Phononic Properties of Two-Dimensional Materials Using Machine Learning Interatomic Potentials. *Applied Materials Today* **2020,** *20*, 100685.
13. Atsushi Togo; Isao Tanaka, First Principles Phonon Calculations in Materials Science. *Scripta Materialia* **2015,** *108*, 1-5.
14. Bohayra Mortazavi; Brahmanandam Javvaji; Fazel Shojaei; Timon Rabczuk; Alexander V. Shapeev; Xiaoying Zhuang, Exceptional Piezoelectricity, High Thermal Conductivity and Stiffness and Promising Photocatalysis in Two-Dimensional $MoSi_2N_4$ Family Confirmed by First-Principles. *Nano Energy* **2021,** *82*, 105716.
15. Xiao Tian; Ying-jie Sun; Jiang-yan He; Xiao-jing Wang; Jun Zhao; Shi-zhang Qiao; Fa-tang Li, Surface P Atom Grafting of g-C_3N_4 for Improved Local Spatial Charge Separation and Enhanced Photocatalytic H_2 Production. *Journal of Materials Chemistry A* **2019,** *7* (13), 7628-7635.
16. Javeed Mahmood; Feng Li; Sun-Min Jung; Mahmut Sait Okyay; Ishfaq Ahmad; Seok-Jin Kim; Noejung Park; Hu Young Jeong; Jong-Beom Baek, An Efficient and pH-Universal Ruthenium-Based Catalyst for the Hydrogen Evolution Reaction. *Nature Nanotechnology* **2017,** *12* (5), 441-446.